🔓 **Open Access**
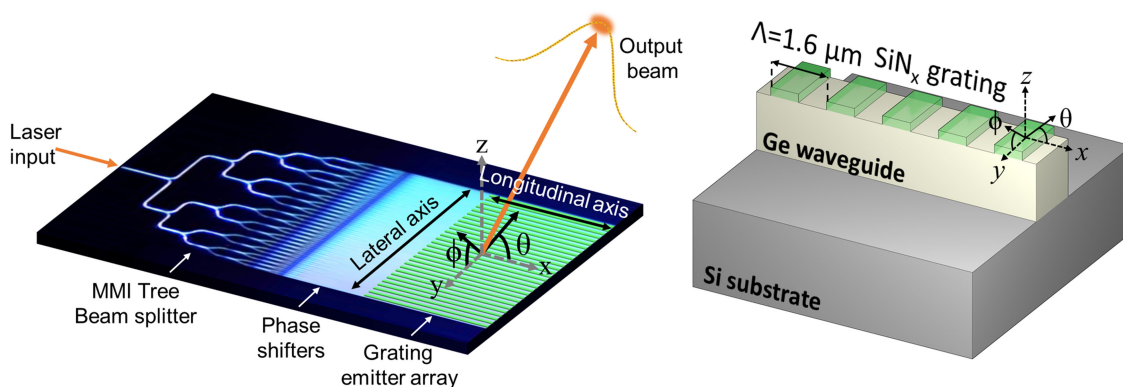
Solid-State MWIR Beam Steering Using Optical Phased Array on Germanium-Silicon Photonic Platform

Mathias Prost
Yi-Chun Ling
Semih Cakmakyapan
Yu Zhang
Kaiqi Zhang
Junjie Hu
Yichi Zhang
S. J. Ben Yoo

Solid-State MWIR Beam Steering Using Optical Phased Array on Germanium-Silicon Photonic Platform

Mathias Prost [ID], **Yi-Chun Ling** [ID]**, Semih Cakmakyapan, Yu Zhang** [ID]**, Kaiqi Zhang, Junjie Hu, Yichi Zhang, and S. J. Ben Yoo** [ID]

Department of Electrical and Computer Engineering, University of California, Davis, CA 95616 USA

Abstract: We demonstrate a chip-scale germanium-silicon optical phased array (OPA) fabricated on a CMOS-compatible platform capable of 2D beam steering in the mid-infrared wavelength range. The OPA included a specially designed grating emitter waveguide array with uniform emission intensity along the *mm*-length waveguide propagation to realize very sharp instantaneous field-of-view (IFOV) and wide beam-steering total-field-of-view (TFOV). The experimental results indicated lateral beam-steering TFOV up to 12.7° by phase-tuning the waveguide array and longitudinal TFOV up to 12° by wavelength tuning. The 3-dB beam divergence is 3.08° × 0.18°. The demonstrated OPA architecture can employ wafer-scale fabrication and integration while supporting sensing and imaging applications in the mid-infrared spectral range.

Index Terms: Optical phased array, silicon photonics, germanium photonics, MWIR, integrated photonic chip, LIDAR, free-space optical communications.

1. Introduction

Optical beam-steering is key to emerging applications such as free-space optical communications (FSOC), active imaging, and light-detection-and-ranging (LIDAR). For example, autonomous systems such as self-driving-vehicles directly benefit from LIDAR devices for mapping the surrounding environment in 3D [1]. Today's LIDAR systems typically rely on bulky optomechanical devices for beam steering purposes. Realizing non-mechanical optical-beam-steering on an integrated solid-state chip-scale module with reduced size and weight opens new possibilities for robust, rapidly-steering, and low-cost LIDAR and FSOC systems [2]. In particular, optical beam steering by solid-state optical phased arrays (OPAs) [3]–[7] is attractive for exploiting well-established semiconductor manufacturing infrastructures. An array of coherent emitters with individual phase control will define and control the near-field pattern, which will also determine the far-field pattern based on Fraunhofer diffraction [8]. As the far-field output beam angle is determined by the slope of the near-field phase, the beam can be steered in the desired direction by controlling the phase of each emitter [9]. Fig. 1 shows a schematic view of an OPA device. To achieve single-lobe far-field pattern and high-resolution beam-steering, the OPA requires a large number of elements (≥thousands) having subwavelength pitch dimensions [10]. Semiconductor photonic integrated circuits (PICs) have strong potentials realizing such OPAs with high integration density exploiting reliable
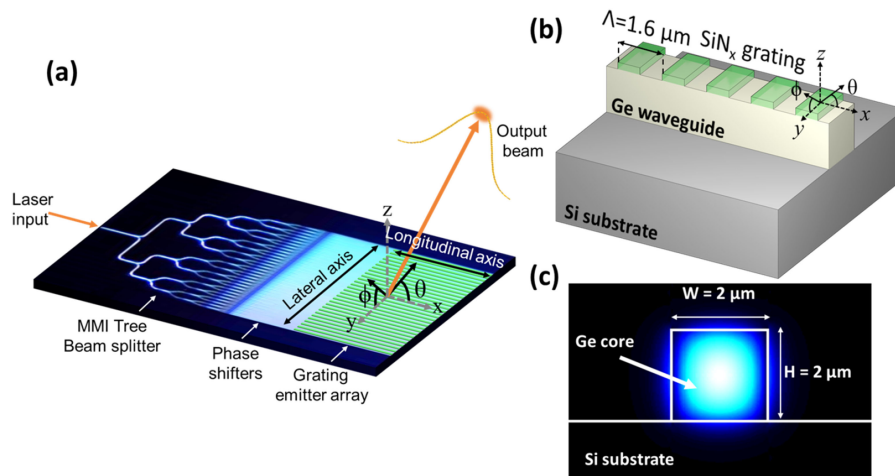
Fig. 1. (a) Schematic view of an OPA PIC based on grating emitter for 2D beam-steering. (b) Used SiNx/Ge-on-Si waveguide stack used for the PIC. (c) Simulated spatial distribution of the TM fundamental mode for the Ge-on-Si waveguide at $\lambda = 4.6$ μm.

fabrication process developed available through semiconductor industry and foundries. The midwave-infrared (MWIR) OPAs are attractive for gas-sensing or thermal LIDARs [11] as well as FSOC overcoming some atmospheric turbulence and scintillation [12], [13]. The MWIR OPAs can also benefit from exploiting the transparent transmission window of the atmosphere and high eye-safety optical power levels for increased ranges. The recent advances of high-efficiency and high-power quantum cascade lasers (QCL) [14] offer the possibility of combining or even integrating compact optical QCL sources with solid-state OPAs. While the mature silicon photonic platform including advanced and complex PICs realized successful shortwave-infrared (SWIR) OPAs with high-quality beam steering results [15]–[17], it is incompatible with MWIR because it includes a silicon oxide layer which strongly absorbs the MWIR radiation. Numerous other solid-state photonic platforms transparent to the MWIR spectral range have been considered; they are III–V materials [18], chalcogenide [19], and silicon-based materials [20]. An attractive candidate we consider here for MWIR OPAs is the germanium-based photonic integrated circuits realized on silicon substrates. Germanium material has a large transparency window from 2 μm to 14 μm and is already widely used in silicon photonics foundry for photodetectors and modulators [21]. Furthermore, the refractive index, the thermo-optical effect coefficient, and the free-carrier effect of germanium are larger than those of silicon, which would benefit of devices with a smaller footprint and better performance. In addition, the fabrication process involving Ge on silicon can utilize the mature wafer-scale CMOS fabrication platform to achieve subwavelength ($\lambda/2$) [22] MWIR structures needed for high-performance LIDARs with reasonable fabrication tolerance and resolution.

In this paper, we demonstrate MWIR optical beam-steering with the OPA PIC realized on a germanium-on-silicon platform fabricated using CMOS-compatible processes. As Fig. 1 illustrates, the OPA PIC consists of a waveguide array with phase-shifter and a grating emitter on each waveguide, receiving light from a distribution network feed by a single laser input. The lateral beam steering is achieved by controlling the optical phase of each grating waveguide of the OPA (phase tilt of the emission plane). The longitudinal beam steering is achieved by varying the wavelength of the laser emission injected into the OPA PIC [23], following the fundamental Bragg reflection law for the radiation direction for a given grating period and wavelength. Compared to the OPA with independent 2D array elements such as spatial light modulators, using such approach allows simplifying the number of elements for the PIC OPA for the required beam steering in longitudinal and lateral directions.

2. Design and Fabrication of Germanium OPA

The Ge-Si OPA PIC relies on four main building blocks: the low-loss optical waveguide and the multimode interferometer (MMI) tree beam-splitter to realize the distribution network, the thermo-optical phase-shifters array to control individually the optical-phase of each channel to determine the far-field pattern of emission, and the *mm*-long grating emitter array to emit the light from the device to the free-space with a large aperture. We decided to use the Ge-on-Si platform for the ease of process fabrication. A more advanced platform such Ge-on-Insulator [24] can offer better performances in terms of light confinement and thermal management, but it needs to add complicated process steps related to layer transfers as wafer bonding and wafer backside removal which were not available to us at this moment with high-yield. The typical wafer stack is shown in Fig. 1(b).

2.1 Photonics Building Blocks Design

We designed all the optical components for single-mode transmission of light in transverse magnetic (TM) polarization to facilitate coupling and future integration with a QCL in the Ge-on-Si waveguides. The single-mode waveguide is based on a Ge strip of a cross-section of $2 \times 2 \ \mu m^2$ on silicon. Fig. 1(c) shows the simulated TM mode profile at $\lambda = 4.6 \ \mu m$ designed using a numerical simulation tool (Lumerical Mode solver) with an effective refractive index of $n_{eff,TM} = 3.89$. The wavelength of $4.6 \ \mu m$ is chosen as a central wavelength because there is a transmission window in the atmosphere for the MWIR at this wavelength. The germanium layer is thick enough to ensure single-mode light propagation and strong confinement without creating process difficulties in case of a thicker layer in terms of stress management and wafer bow. The waveguide bending radius is set to a conservative value of $50 \ \mu m$ in order to minimize the bending loss. Based on these waveguide parameters, we designed a 1×2 MMI 3 dB beam-splitter formed by a rectangular multimode region of $35.5 \times 9 \ \mu m^2$ ($L \times W_M$). The pitch between the two output waveguides is $4.8 \ \mu m$. The input and output waveguides are linearly tapered from $2 \ \mu m$ to $3 \ \mu m$ along a length of $50 \ \mu m$ to ensure efficient light coupling to the multimode region. Based on our previous work for the silicon photonics platform [25], we designed a SiN_x assisted germanium grating with uniform emission intensity over a 1.5-mm length as depicted in 1(b). Long grating leads to a sharp instant field of view (IFOV) in the far-field patterns. The grating coupling coefficient (κ) must be relatively low at the input of the waveguide and increase linearly with the propagation length to achieve uniform optical emission from the grating along the length of the waveguide. The duty cycle of the grating modulates this parameter as the coupling strength is depending on the geometry of the perturbation element [25]. To further enhance the dynamic range of the variations in κ values while keeping the dimensions of the grating elements (SiN_x) and the gap between them within the fabrication tolerance, we have also varied the grating element width in order to keep the waveguide propagation constant to be the same along the waveguide [25]. The design allows uniform intensity and constant emission angle across the relatively long emission length (mm) for the given wavelength. The grating design comprises a 160 nm thick of SiN_x overlayer on the Ge $2 \times 2 \ \mu m^2$ wire waveguide. The grating period is $\Lambda = 1.6 \ \mu m$, which corresponds to a center output angle of $45°$ at $4.6 \ \mu m$ [26] as shown from the element factor in the far-field in Fig. 2(c). The duty cycle Δ is linearly tuned from 0.81 to 0.5 while the width is increased from 600 nm to $2 \ \mu m$. Fig. 2(a) and (b) show the results of Finite-Difference Time-Domain (FDTD) simulation of transmitted upward power along the waveguide for 0.5 mm propagation length. The value of the simulated propagation length is limited by computation time. The custom grating design can achieve uniform emission over mm-length propagation using linear apodization.

2.2 OPA Design and Properties

For the phase-calibration, we decided to use thermo-optical effect for the phase-shifter as it induces no additional optical losses and it is simple to implement. On the other hand, since we have grating emitters on the waveguides, we cannot place heaters over the waveguides with sufficient spatial
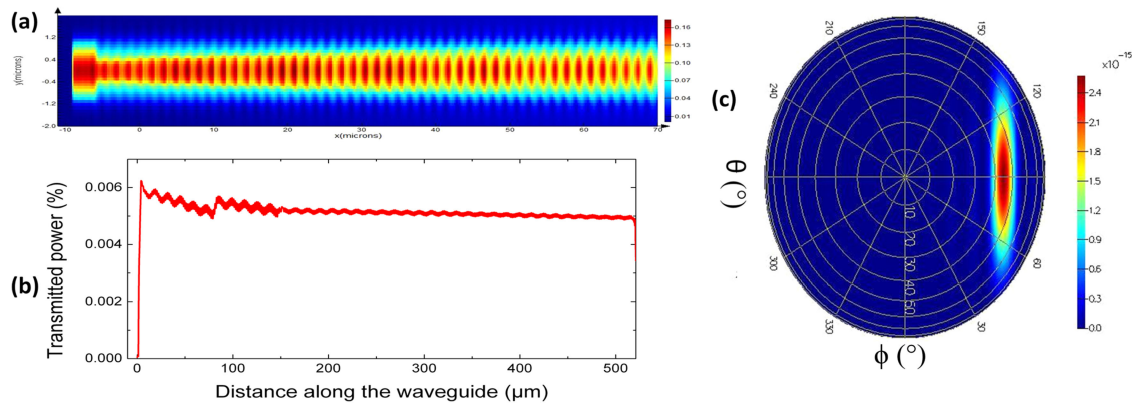
Fig. 2. (a) Top monitor of the electric near-field profile along with the waveguide grating emitter for 40 periods. (b) Optical upward transmitted power along the propagation direction for apodized grating of 500 μm length. (c) Far-field element factor of the grating emitter at $\lambda = 4.6$ μm showing emission at a 45° angle.
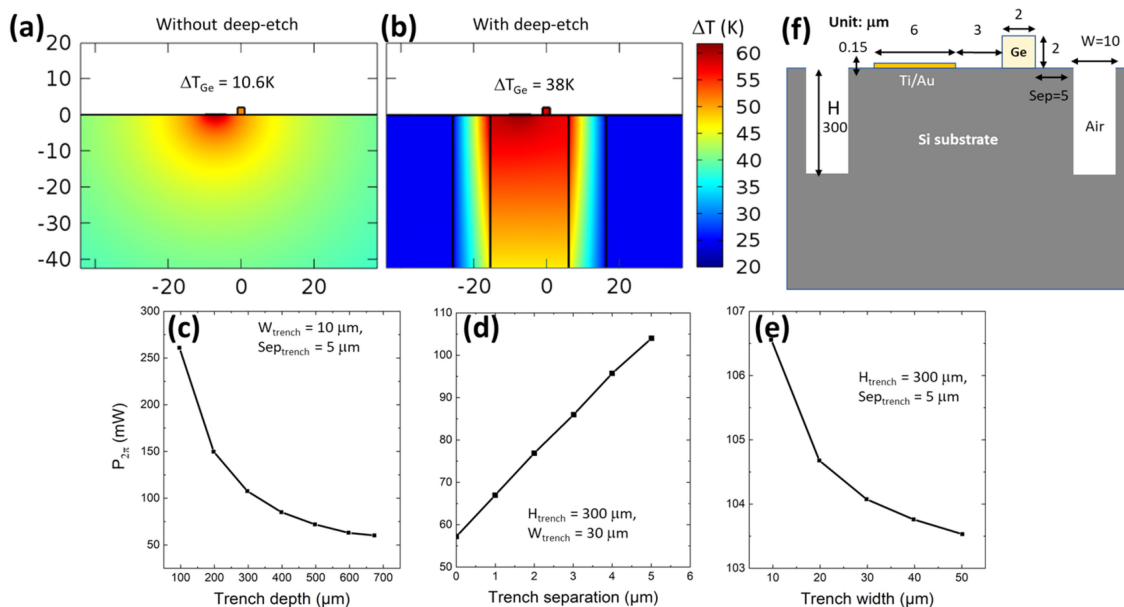

Fig. 3. Phase-shifter cross-section. (a) Thermal simulation of a heating element without isolation trenches, (b) with isolations trenches, (c) effect of isolation trenches depth. (d) Isolation trenches separation, and (e) trenches width on 2π phase-shift power value. (f) Final cross-section of the thermal-phase shifter.

separation to avoid large optical loss due to the metal absorption. We decided to use the structure shown in Fig. 3(a), where the Ti/Au resistive heater will heat the Ge-on-Si waveguide laterally. Since the substrate is acting as a heat-sink, the deep trenches help isolate and confine the heat laterally. We simulated the thermal module using COMSOL to determine the power needed to achieve a 2π phase-shift for 1 mm Ge-on-Si waveguide propagation at 4.6 μm wavelength. As Fig. 3(a) shows, if there were no trenches, the power needed is about 980 mW which is impractical to be used for an array of many phase-shifters. On the other hand, Fig. 3(c), (d) and (e) show, the required power for 2π phase-shift reduces by more than an order of magnitude by adding the deep trenches with more than 200 μm depth and 20 μm width with a separation of 5 μm from the waveguide. Moreover, the trenches help reduce the thermal cross-talk in a configuration of the thermal phase array. For
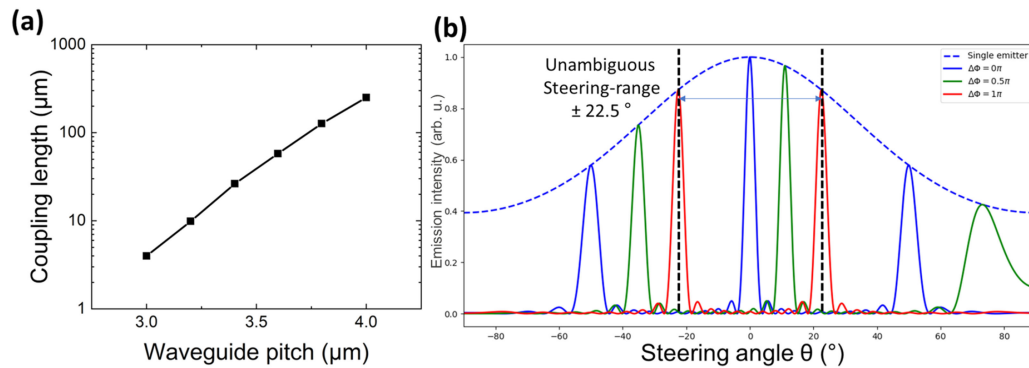
Fig. 4. (a) 10% Waveguide cross-talk length versus waveguide pitch at 4.6 μm. (b) Array factor of Ge-OPA for 6 μm pitch and 12 channels with different phase configuration.

a 200 μm pitch separation between neighboring phase-shifters, the thermal crosstalk between the waveguides is reduced from 25% for the OPAs without trenches to less than 0.1% with the trenches.

Due to the limitation of the number of channels achievable using our in-house wire-bonding, we limited the OPA channels to a number of 12, i.e., the two outer channels on both sides of the 16 channels MMI splitter tree are not routed to the grating section but are used for alignment purpose and phase-shifter calibration.

Three factors drove the choice for the OPA waveguide pitch. The waveguide crosstalk, the unambiguous steering range, and the beam-spot size. According to numerical simulations shown in Fig. 4(a), less than 10% crosstalk only occurs after 1 cm propagation length for pitch larger than 3.2 μm. Above this pitch, the cross-talk error is relatively low for cm-long emitter compared to propagation losses, but the unambiguous steering range will be reduced because of the positions of the grating-lobes become closer to the main lobe. In our experiment, the observable beam steering range will be limited by the back focal plane imaging setup in the MWIR. A relaxed pitch to avoid phase error due to waveguide crosstalk without observations of the grating-lobes is considered. Furthermore, the number of channels that we can address to control the phase-shifters is limited by the in-house wire bonding packaging step. In consideration of these two limitations, we decided to fix the pitch at 6 μm in order to make the far-field spot narrower as the aperture size of the OPA is increased. It allows an unambiguous beam steering range of $+/-22.5°$ with an expected 3 dB diffraction-limited spot size estimated to 3.2° in the lateral direction as shown in Fig. 4(b). For 1.5 mm grating length, the expected 3 dB size diffraction-limited spot size in the longitudinal direction is 0.15°.

2.3 Process Fabrication of Germanium Based Photonics Devices

We started the fabrication process by thin-film hetero-epitaxy of germanium on a silicon wafer using a Reduced-Pressure Chemical Vapor Deposition (RPCVD) reactor (Epi 200 Centura from Applied Materials). Due to the lattice mismatch between the two materials, we used a two-steps growth temperature to ensure high-quality epitaxial germanium thin-film on silicon [27]. After the growth of 2 μm thick Germanium layer, the wafer is in-situ annealed in the chamber under H_2 atmosphere up to 850 °C to mitigate the threading dislocation density. Then the wafer is transferred out to a Plasma-Enhanced Chemical Vapor Deposition (PECVD) reactor to deposit the grating material. A 160 nm thick film of SiN_x is deposited on top of the germanium layer at 350 °C using NH_3 and SiH_4 reactive gases. The wafer is subsequently patterned using Deep-UV projection lithography to form the grating (ASML 5500/300). The SiN_x layer is fully etched using C_4F_8/H_2 gas mixture in an Inductively Coupled Plasma Reactive-Ion Etching (ICP-RIE) chamber. The etch-selectivity between SiN_x and Ge has been calibrated to avoid the over-etch in the germanium that can lead to stronger grating emission strength than the original design. Subsequently, after photoresist cleaning, the wafer is exposed by the DUV projection lithography to pattern the waveguide layer aligned to
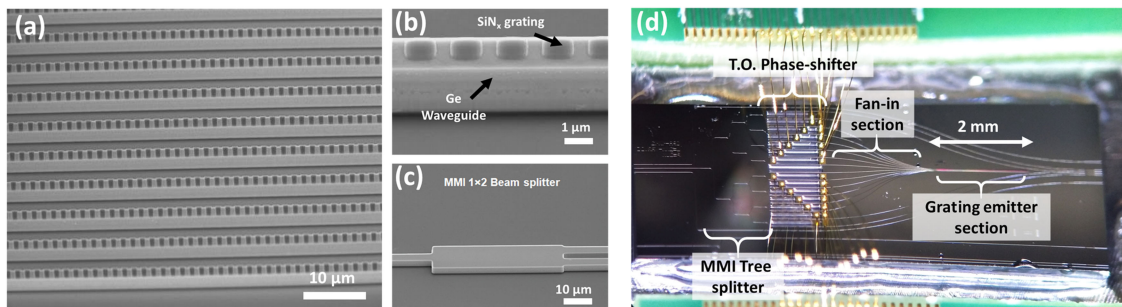
Fig. 5. (a) SEM picture of grating emitter waveguide array viewed from a 45° angle. (b) Detailed view of a Ge waveguide with SiNx grating on top. (c) SEM picture of a MMI 1 × 2 beam splitter. (d) Microscope picture of a packaged 12 channels OPA beam-steering experiments in the MWIR.

the grating layer. The alignment tolerance from the stepper lithography tool is 150 nm maximum between two layers. To avoid any corrugation on the waveguide due to SiN_x masking during the Ge etching, the SiN_x etching process is run again to clear any remaining SiN_x if misalignment occurs. Then, the germanium layer is etched down to the Si substrate using a HBr/Cl_2 gas mixture in an ICP-RIE chamber. The thermo-optic phase shifters are then fabricated. First, we performed a deep-etch of trenches down to 200 μm in the silicon substrate between each waveguide. The trenches will confine the heat in the Ge waveguide by limiting the thermal conduction to the Si substrate and will minimize the thermal crosstalk from adjacent channel waveguide. Then the metal heaters are defined by a lift-off process. We deposited a Ti/Au metal line of 1 mm × 4 μm × 200 nm ($L \times W \times h$) on the Si substrate spaced of 3 μm from the germanium waveguide. We choose this metal stack for the ease of fabrication, but it can easily be replaced by any other metal like TiN or W that are CMOS process compatible. Fig. 5(a) shows a detailed view of the grating waveguide array using scanning electron microscopy (SEM). After completing the fabrication, the wafer is diced into chips and packaged on a printed circuit board (PCB). The metal pad input ports of the phase-shifter are wire-bonded to allow electrical connection to the digital-analog converter (DAC) control system. Each thermo-optical phase shifter port is connected to a distinct ground line to avoid current overload on the metal line of the chip. Fig. 5(d) shows a fully packaged beam-steering device with 12 channels array.

3. Characterization and Results of Beam-Steering in the MWIR

Characterization of the fabricated devices utilized a tunable MWIR source (a tunable QCL from Day-light Solutions) operating in continuous wave in our experimental apparatus. The laser can provide a maximum peak intensity of 200 mW at the 4.6 μm center wavelength with a tuning capability range of 180 nm to enable beam-steering scan in the longitudinal direction. The light is coupled from the QCL source to the 10 μm wide tapered input waveguide using molded aspheric lens transparent in the MWIR with a high numerical aperture (N.A. = 0.64). In the first place, we characterized, the germanium waveguide optical properties using a testing chip from the same fabrication batch. The waveguide loss propagation is calculated by the cut-back method, in which we measured the transmission of four spiral waveguides with lengths of 2.5, 4.5, 6.5 and 8.5 cm. The spirals have the same number of turns. By a linear fit, we extracted an average optical propagation loss of 1.6 ± 0.7 dB/cm over the 4.55–4.60 μm spectral range. Subsequently, we experimentally evaluated the performance of the thermo-optic phase shifters. We fabricated an asymmetric Mach Zehnder Interferometer (MZI) with a fixed path length difference of 225 μm. The resulting free spectral range (FSR) is approximately 23 nm at the 4.6 μm wavelength. We experimentally measured a value of 104 ± 14 mW to achieve a 2π phase shift, which is in good agreement with the numerical simulations where a value of 106 mW is expected for the trenches design.
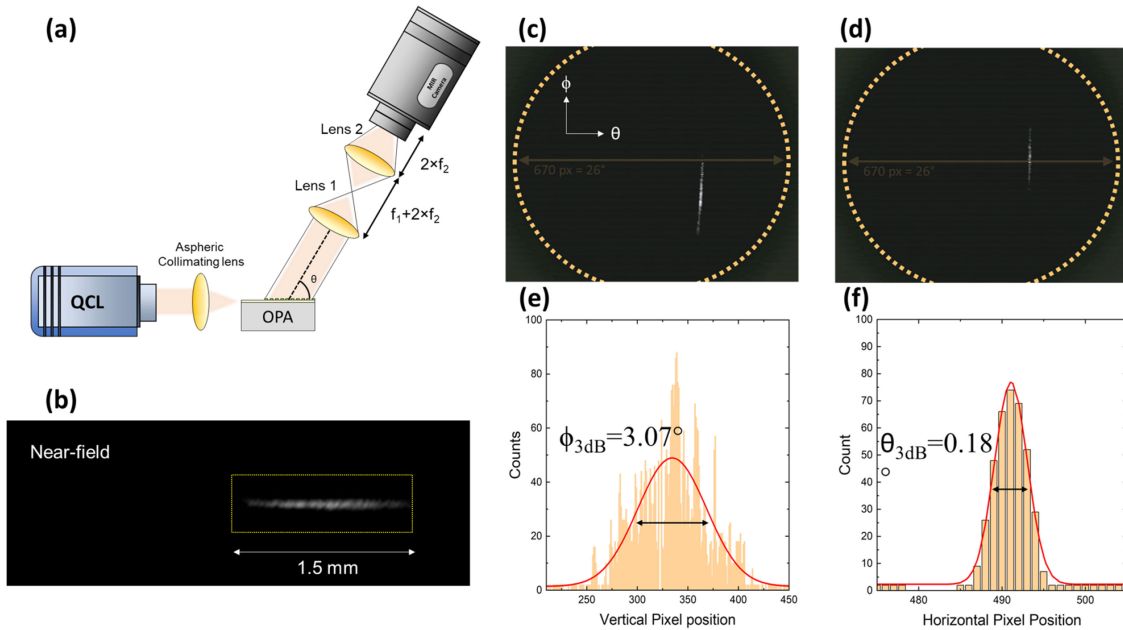
Fig. 6. (a) Schematic of far-field measurement setup using tube lens setup. (b) Captured near-field of the OPA showing the emission profile using a single lens setup. (c) Imaged far-field spot before and (d) after phase-error correction. The circle dashed line shows the acceptance angle of the setup, (e) extracted lateral intensity profile and (f) longitudinal intensity profile after P.E.C. at $\lambda = 4.6$ μm. The solid red plot is the Gaussian curve fit used to measure the 3 dB beam divergence.

After characterizing the different base optical components of the PIC, we proceeded to the beam-steering experiment using an OPA with 12-channels and a waveguide pitch of 6 μm. To image the emitted light from the OPA in the far-field, we used a lens tube with a set of two aspheric ZnSe lenses coupled to a MWIR camera (FLIR A6700) as depicted in Fig. 6(a). The collection system is tilted by an angle of 45° from the normal of the chip to closely match the direction of the emitted light at the center wavelength. Prior to the experiment, we calibrated the angle value using a rotating mirror setup that steers a collimated laser beam to reproduce the beam-steering experiment with a known angle. We found a correspondence of 0.038°/px. The acceptance angle of the setup is ±13° due to the limitation of the collecting lens having a low numerical aperture (N.A. = 0.22) with 50 mm working distance to have sufficient clearance with the device. The chip is mounted on the test-bench and the light is coupled to the OPA, and the alignment is optimized using one monitoring output waveguide. Fig. 6(b) shows the near-field pattern of the grating emitter when using a single lens setup imaging without any exponential decay over 1.5 mm propagation length. The array delivers a relative uniform emission pattern thanks to the apodization of the grating coupling strength. Inherent optical path length difference due to fan-in routing from the phase-shifter to the OPA and process non-uniformity of the waveguide will result in phase-errors that will distort the beam as seen in Fig. 6(c). We applied a machine learning algorithm [28] that uses the feedback from the camera to control the phase-shifters to optimize the phase-tuning setting. Thus, it applies a phase-error correction (PEC) that removes background peaks of the far-field beam as shown in Fig. 6(d) and center the beam back to the origin. From this calibrated beam, we measured the 3 dB beamwidth divergence in lateral axis ϕ to be 3.07° and in longitudinal axis θ to be 0.18° as depicted in Fig. 6(e) and (f) which is matching closely the diffraction-limited calculation for the given OPA dimensions. The beam in the longitudinal axis is sharper thanks to the long aperture of the custom grating emitter. In the lateral direction, the beam is broadened due to the small number of channels for this OPA. A rounded beam can be achieved in the future by scaling the number of channels. We didn't observe grating-lobes as the unambiguous beam-steering range is larger than the acceptance angle of the setup.
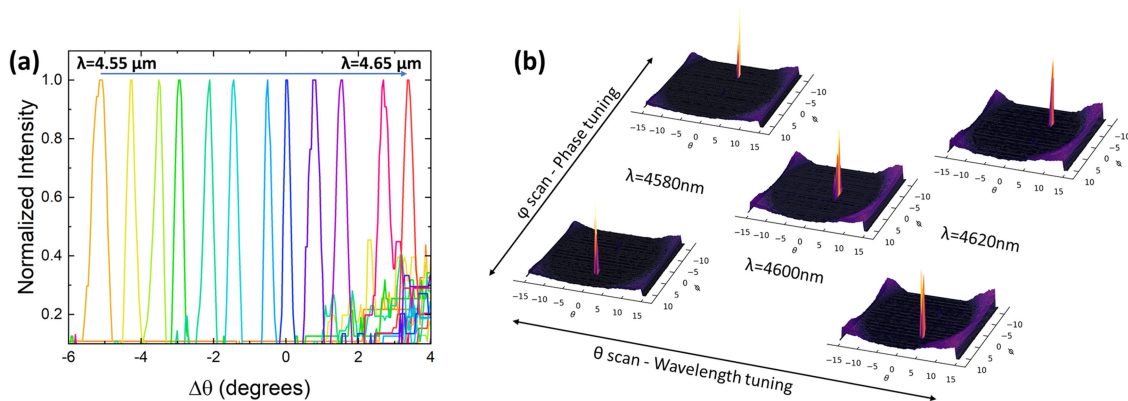
Fig. 7. (a) Normalized far-field scans along the θ axis for different input wavelength from 4500 nm to 4650 nm. (b) Collection of wavelength and phase tuning plot to achieve 2D beam-steering.

Fig. 7(a) shows a collection of far-field scans along the θ axis for different input wavelengths. We experimentally achieved a beam steering of 12° in the longitudinal direction limited by the wavelength tuning range of the QCL. For angles larger than 4°, the signal-noise ratio starts to be important due to the proximity of the beam with the edge of the camera sensor. It created an undesired background noise. The position of the peak is still possible to extract, but not shown on the figure for readability. We found a steering angle tunability versus the wavelength in the θ axis of 0.069°/nm. This value is larger than the one predicted from the group index simulations due to fabrication error and material refractive index variation of the SiN$_x$ layer in the MWIR. A two-dimensional far-field measurement was made using different sets of phase and wavelength tuning as shown in Fig. 7(b). The OPA is controlled to steer the beam in the longitudinal and the lateral direction. We achieved a steering range up to 12.7° in the longitudinal direction by phase-tuning.

4. Conclusion

We demonstrate, for the first time to our knowledge, a solid-state 2D beam-steering device in the MWIR. The custom SiN$_x$/Ge grating maintains uniform propagation constant over a 2-mm length. It leads to sharp beam-divergence down to 0.18° in the perpendicular direction with wavelength tunability of 0.069°/nm. In the lateral direction, we were able to demonstrate a beam-steering angle of 12.7° by phase tuning and a beam divergence 3.07°. These values can be easily enhanced by increasing the total number of channels and by reducing the pitch of the OPA waveguide. Such a beam-steering device enables new applications in LIDAR and FSOC. Monolithic or hybrid integration with the laser source is possible through progress in the complementary work of the monolithically integrated tunable quantum cascade laser [29].

Acknowledgment

References

[1] "LiDAR drives forwards," *Nature Photon.*, vol. 12, no. 8, pp. 441–441, 2018.
[2] S. R. Davis *et al.*, "A lightweight, rugged, solid state laser radar system enabled by non-mechanical electro-optic beam steerers," *Proc. SPIE*, vol. 9832, pp. 186–196, 2016, Art. no. 98320K.
[3] C. V. Poulton *et al.*, "Large-scale silicon nitride nanophotonic phased arrays at infrared and visible wavelengths," *Opt. Lett.*, vol. 42, no.1, pp. 21–21.
[4] S. Chung, H. Abediasl, and H. Hashemi, "A monolithically integrated large-scale optical phased array in silicon-on-insulator CMOS," *IEEE J. Solid-State Circuits*, vol. 53, no. 1, pp. 275–296, Jan. 2018.

[5] D. N. Hutchison *et al.*, "High-resolution aliasing-free optical beam steering," *Optica*, vol. 3, no. 8, pp. 887–887, 2016.

[6] D. Kwong *et al.*, "On-chip silicon optical phased array for two-dimensional beam steering," *Opt. Lett.*, vol. 39, no. 4, pp. 941–941, 2014.

[7] J. C. Hulme *et al.*, "Fully integrated hybrid silicon two dimensional beam scanner," *Opt. Exp.*, vol. 23, no. 5, pp. 5861–5861, 2015.

[8] M. Born and E. Wolf, *Principles of Optics*, 7th ed. Cambridge, U.K.: Univ. Cambridge Press, 1999.

[9] M. J. R. Heck, "Highly integrated optical phased arrays: Photonic integrated circuits for optical beam shaping and beam steering," *Nanophotonics*, vol. 6, pp. 152–152, 2017.

[10] C. A. Balanis, *Antenna Theory: Analysis and Design*. Hoboken, NJ, USA: Wiley, 2005.

[11] P. F. Ambrico *et al.*, "Sensitivity analysis of differential absorption lidar measurements in the mid-infrared region," *Appl. Opt.*, vol. 39, no. 36, pp. 6847–6865.

[12] E. Leitgeb et al. "Analysis and evaluation of optimum wavelengths for free-space optical transceivers," in *Proc. 12th Int. Conf. Transparent Opt. Netw.*, 2010, pp. 1–7.

[13] P. Corrigan et al. "Quantum cascade lasers and the Kruse model in free space optical communication," *Opt. Exp.*, vol. 17, no. 6, 2009, pp. 4355–4359.

[14] Y. Bai *et al.*, "Room temperature quantum cascade lasers with 27% wall plug efficiency," *Appl. Phys. Lett.*, vol. 98, no. 18, pp. 181102–181102, 2011.

[15] W. Xie *et al.*, "Heterogeneous silicon photonics sensing for autonomous cars," *Opt. Exp.*, vol. 27, no. 3, pp. 3642–3663, 2019.

[16] C. V. Poulton *et al.*, "Coherent solid-state LIDAR with silicon photonic optical phased arrays," *Opt. Lett.*, vol. 42, no. 20, pp. 4091–4091, 2017.

[17] Y. Zhang *et al.*, "Sub-wavelength-pitch silicon-photonic optical phased array for large field-of-regard coherent optical beam steering," *Opt. Exp.*, vol. 27, no. 3, pp. 1929–1940, 2019.

[18] R. Wang *et al.*, "III–V-on-silicon photonic integrated circuits for spectroscopic sensing in the 2–4 m wavelength range," *Sensors*, vol.17, no. 8, pp. 1788–1788, 2017.

[19] H. F. Ma, B. G. Cai, T. X. Zhang, Y. Yang, W. X. Jiang, and T. J. Cui, "Three-dimensional gradient-index materials and their applications in microwave lens antennas," *IEEE Trans. Antennas Propag.*, vol. 61, no. 5, pp. 2561–2569, May 2013.

[20] R. Soref, "Mid-infrared photonics in silicon and germanium," *Nature Photon.*, vol. 4, pp. 495–495, 2010.

[21] V. Reboud *et al.*, "Germanium based photonic components toward a full silicon/germanium photonic platform," *Prog. Cryst. Growth Characterization Mater.*, vol. 63, no. 2, pp. 1–24, 2017.

[22] P. Cheben *et al.*, "Subwavelength integrated photonics," *Nature*, vol. 560, no. 7720, pp. 565–572, 2018.

[23] J. K. Doylend *et al.*, "Two-dimensional free-space beam steering with an optical phased array on silicon-on-insulator," *Opt. Exp.*, vol. 19, no 22, pp. 21595–21604, 2011.

[24] J. Kang, M. Takenaka, and S. Takagi, "Novel Ge waveguide platform on Ge-on-insulator wafer for mid-infrared photonic integrated circuits," *Opt. Exp.*, vol. 24, no. 11, pp. 11855–11864, 2016.

[25] K. Shang *et al.*, "Uniform emission, constant wavevector silicon grating surface emitter for beam steering with ultra-sharp instantaneous field-of-view," *Opt. Exp.*, vol. 25, no. 17, pp. 19655–19655, 2017.

[26] K. Okamoto, *Fundamentals of Optical Waveguides*. New York, NY, USA: Academic, 2006.

[27] J. M. Hartmann *et al.*, "Epitaxial growth of Ge thick layers on nominal and 6° off Si(0 0 1); Ge surface passivation by Si," *Semiconduct. Sci. Technol.*, vol. 24, no. 5, 2009, Art. no. 055002.

[28] T. Komljenovic and P. Pintus, "On-chip calibration and control of optical phased arrays," *Opt. Exp.*, vol. 26, no. 3, pp. 3199–3199.

[29] S. Slivken, D. Wu, and M. Razeghi, "Monolithic beam steering in a mid-infrared, surface-emitting, photonic integrated circuit," *Sci. Rep.*, vol. 7, no. 1, 2017, Art. no. 8472.